Applied Catalysis B: Environmental 322 (2023) 122076

Contents lists available at ScienceDirect

Applied Catalysis B: Environmental

journal homepage: www.elsevier.com/locate/apcatb

Insights into the removal of chloramphenicol by electrochemical reduction on Pd/NiFe-MOF/foam-Ni electrode: Performance and mechanism

Junjing Li [a,*], Shumin Ma [a], Ziyan Qi [a], Jing Ding [b], Menghua Yin [a], Bin Zhao [a], Zhaohui Zhang [a], Yu Wang [a], Hongwei Zhang [a], Liang Wang [a,*], Dionysios D. Dionysiou [c]

[a] School of Environmental Science and Engineering, Tiangong University, State Key Laboratory of Separation Membranes and Membrane Processes, Binshui West Road 399, Xiqing District, Tianjin 300387, PR China
[b] School of Environment, Harbin Institute of Technology, Huanghe Road 73, Nangang District, Harbin 150090, PR China
[c] Environmental Engineering and Science Program, Department of Chemical and Environmental Engineering (ChEE), University of Cincinnati, Cincinnati, OH 45221-0012, USA

ARTICLE INFO

Keywords:
Pd/NiFe-MOF/foam-Ni
Metal-organic framework
Electrocatalytic hydrodechlorination
Chloramphenicol
Active atomic hydrogen

ABSTRACT

To effectively improve the particle dispersion of the catalytic metal and catalytic activity of the palladium electrode, a new type of efficient Pd/NiFe-MOF/foam-Ni composite electrode was prepared. The results showed that the reaction rate constant of chloramphenicol (CAP) by Pd/NiFe-MOF/foam-Ni was three times that of Pd/foam-Ni. X-ray absorption fine structure (XAFS) results showed that palladium on Pd/NiFe-MOF/foam-Ni had a lower oxidation state than that on Pd/foam-Ni. The Pd nanoparticles were uniformly dispersed on the composite electrode and had a small particle size. The electrode had good resistance to sulfites and the electrocatalytic activity was hardly affected in the presence of Cl^-, NO_3^-, HCO_3^-, CO_3^{2-} and Ca^{2+} in wastewater. Besides, the introduction of nickel-iron bimetallic organic framework (NiFe-MOF) increased the electron density of Pd, improved the dispersion and electrochemical active surface area (ECSA) of Pd. The reaction pathway of CAP was proposed, and the ecotoxicity of CAP and its products was evaluated by the Ecological Structure Activity Relationships (ECOSAR) model. Combined experimental data and density functional theory (DFT) analysis enable us to propose the hydrodechlorination mechanism of CAP on the Pd/NiFe-MOF/foam-Ni electrode. The Pd/NiFe-MOF/foam-Ni composite electrode has good application prospects in the treatment of organic pollutants in wastewater and other environmental remediation applications.

1. Introduction

In the past ten years, the increasing pollution caused by the increase amounts of pharmaceuticals and personal care products (PPCPs) used around the world has raised concern regarding their impacts on human health and the living environment [1–5]. It is estimated that the annual consumption of antibiotics alone in the world is between 100,000 and 200,000 tons [4,6]. Among them, chloramphenicol (CAP) is commonly used as antibiotic against bacterial infections. It is frequently detected in surface and underground water, wastewater effluents, and soil environment [7–9]. According to the flux estimation, about 2.07 tons of CAP are discharged into the Yangtze River Basin per annum [10]. CAP has blood toxicity, embryotoxicity, and strong immunosuppression and can even affect the physiological functions of animals, plants, and microorganisms [11–15]. Therefore, it is urgent to develop effective technologies and methods to remove CAP and other chlorinated antibiotics to reduce environmental pollution.

At present, nano zero valent iron is a method for in-situ remediation of chloramphenicol polluted water, scholars have done a lot of work [16–18]. However, it has some limitations due to its instability and easy agglomeration. Electrocatalytic hydrodechlorination technology uses the reductive active atomic hydrogen (H*) produced by cathode materials in the electrochemical reaction as the reducing agent to cause the dechlorination and hydrogenation of chlorine-containing pollutants and to reduce their toxicity [19]. This technology has been gradually applied in groundwater and wastewater treatment due to its low risk of secondary pollution, high reaction rate, and convenient operation [20,21]. Palladium (Pd) has been regarded as the preferred catalyst for electrocatalytic hydrodechlorination due to its ability to adsorb hydrogen and generate H* [22–25]. However, the phenomenon of easy agglomeration

* Corresponding authors.
E-mail addresses: junjingli85@163.com (J. Li), mashi7822@163.com (L. Wang).

https://doi.org/10.1016/j.apcatb.2022.122076
Received 3 May 2022; Received in revised form 19 September 2022; Accepted 12 October 2022
Available online 15 October 2022

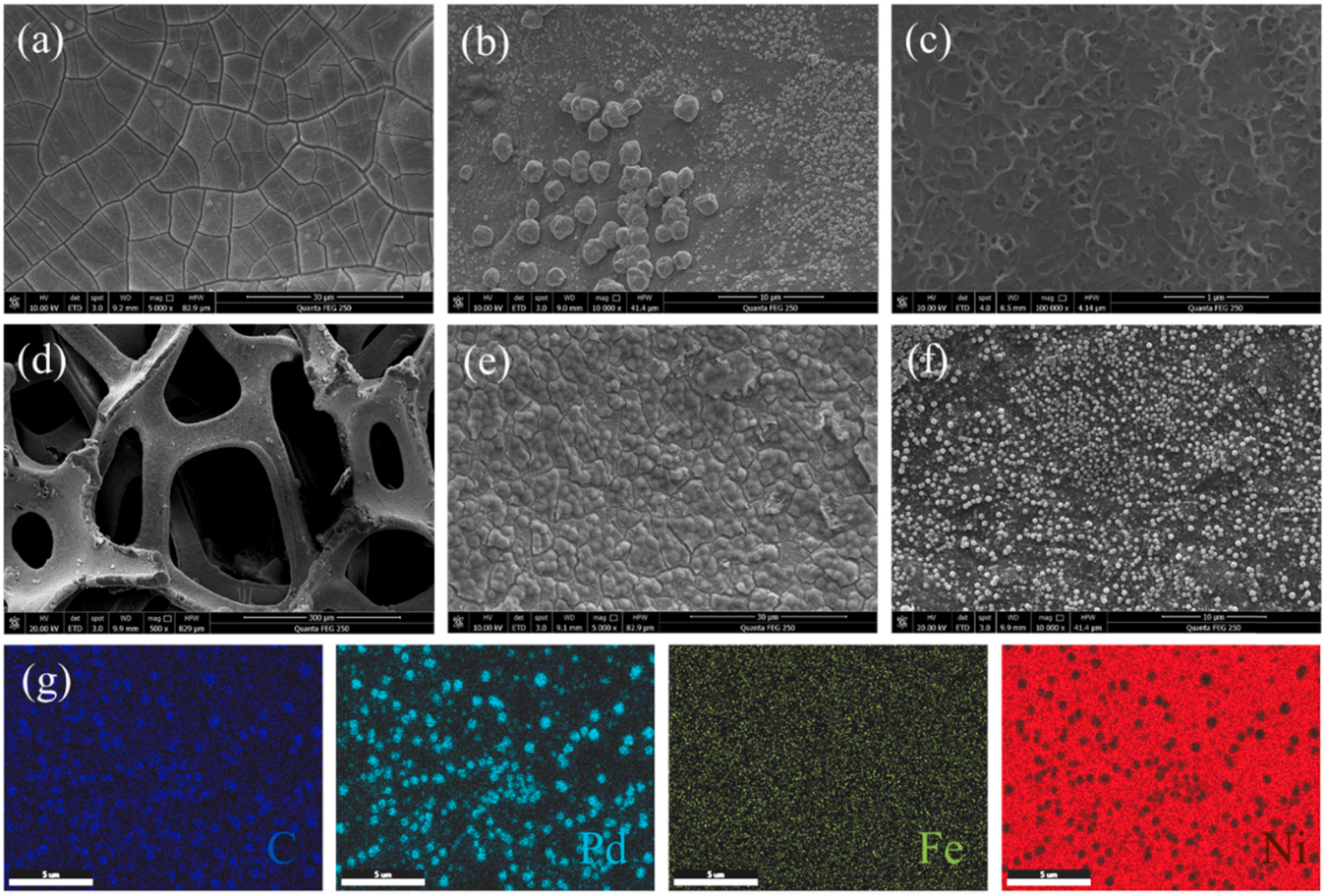

Fig. 1. SEM images of (a) foam-Ni, (b) Pd/foam-Ni, (c) NiFe-MOF/foam-Ni, Pd/NiFe-MOF/foam-Ni (d) 500 × , (e) 5000 × , (f) 10000 × ; (g) The corresponding EDS elemental mapping of Pd/NiFe-MOF/foam-Ni.

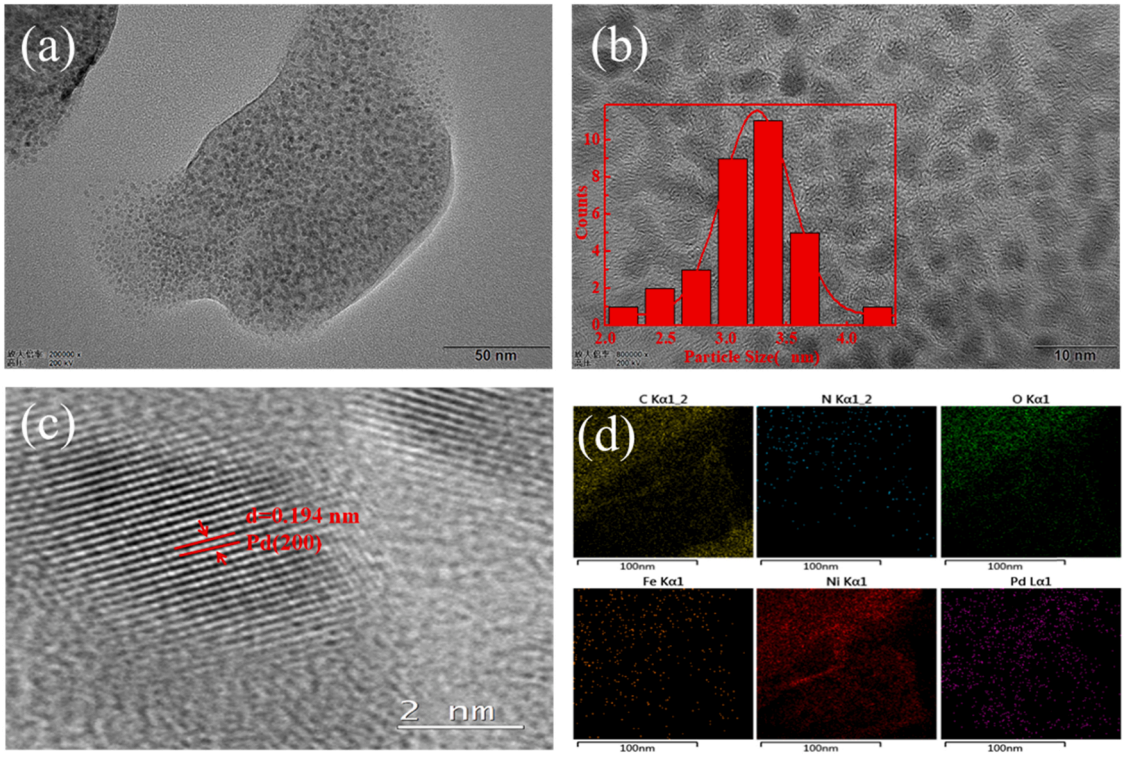

Fig. 2. (a) TEM images and (b) particle size distribution histogram of Pd/NiFe-MOF/foam-Ni; (c) HRTEM; (d) The EDS of Pd/NiFe-MOF/foam-Ni electrode.

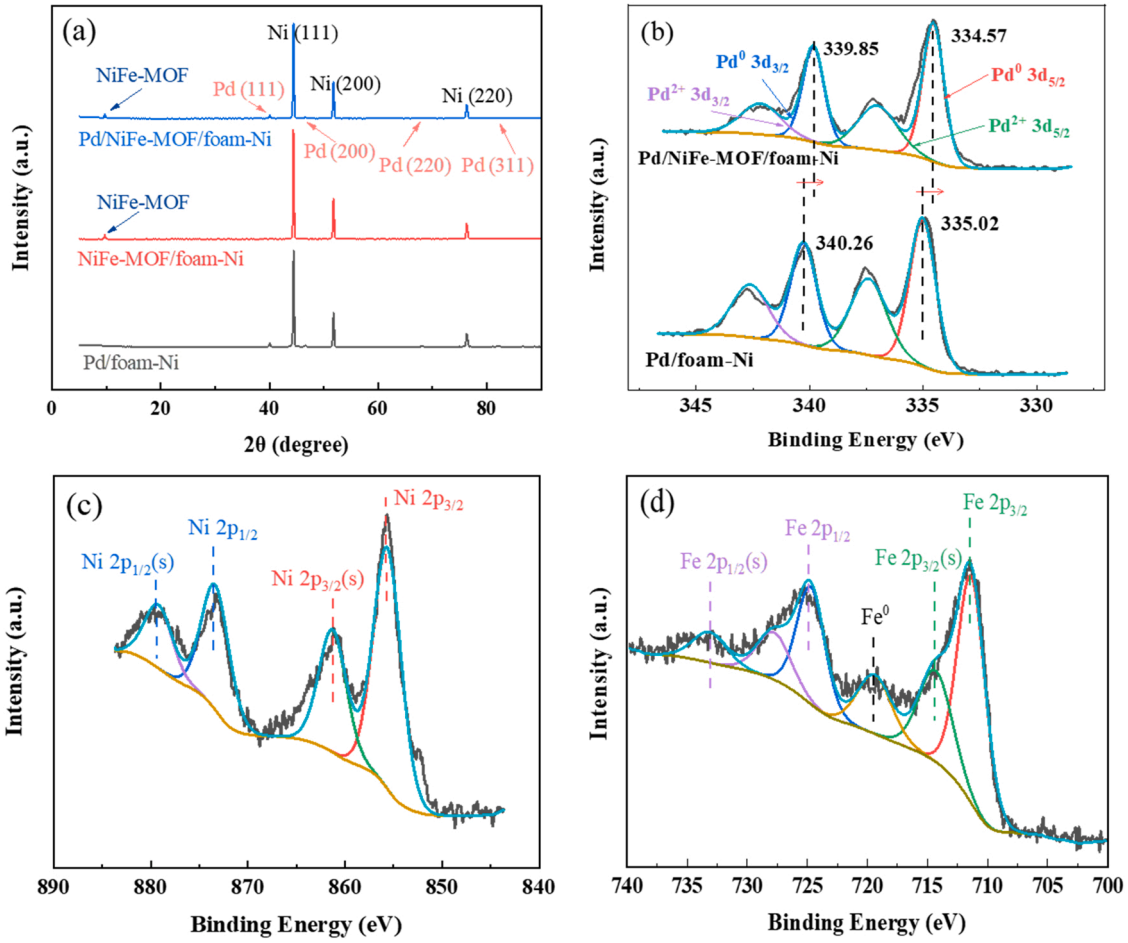

Fig. 3. (a) The XRD patterns of Pd/foam-Ni, NiFe-MOF/foam-Ni and Pd/NiFe-MOF/foam-Ni electrode; (b) Pd 3d XPS spectra of Pd/foam-Ni and Pd/NiFe-MOF/foam-Ni electrode; (c) Ni 2p, (d) Fe 2p of Pd/NiFe-MOF/foam-Ni.

of Pd particles has led to the researches on improving its utilization efficiency and reducing its aggregation [26,27].

Metal-organic frameworks (MOFs) are multifunctional porous materials that have high porosity and high specific surface area [28,29]. The porous structure facilitates the diffusion of water molecules and the release of gaseous substances [30–32], while high specific surface area promotes the dispersion of metal catalysts. In general, metal catalysts can be highly dispersed on the surface of MOFs. Jiang et al. [33] found that NMNC/2D MOF hybrids improved the dispersion of noble metal components and produced an excellent performance for the oxygen evolution reaction. Wan et al. [34] proposed that the Co/NCNTs/NSs developed by pyrolyzing Co/Zn-MOF nanosheets could highly expose the active surface and enhance the mass transfer kinetics and electrical conductivity. The nickel-iron bimetallic organic framework (NiFe-MOF) is a metal-organic skeleton that has a high specific surface area, high porosity, good conductivity, and a three-dimensional porous structure. Such a structure is not only conducive to the loading of other materials but also provides more active sites for the electrocatalytic reaction and water splitting [35–37]. Therefore, it is expected to alleviate the problems of aggregation of Pd and promote hydrodechlorination in this study by using MOF as the intermediate layer and increasing the specific surface area of the electrode. Based on the properties of MOFs, we hypothesize to observe a synergistic effect of MOFs and Pd on electrocatalytic hydrodechlorination.

In this paper, NiFe-MOF was added between Pd and the matrix as an intermediate layer to improve the dispersion of the metal catalyst and the electrocatalytic performance of the electrode. A new type of Pd/NiFe-MOF/foam-Ni composite electrode was prepared, and the apparent morphology, electrode structure, and electrochemical properties of the Pd/NiFe-MOF/foam-Ni electrode were analyzed. By measuring the electrochemical active surface area (ECSA) and partial characterization results, the effect of the intermediate layer NiFe-MOF and its influence on the catalytic effect of the electrode system were studied. The major active hydrogen species in the electrocatalytic hydrodechlorination process were investigated. The electronic structure and coordination environment of Pd were probed by X-ray absorption fine structure (XAFS). The reaction pathway of CAP by Pd/NiFe-MOF/foam-Ni electrode was elucidated, and the ecotoxicity of its reaction products was assessed. In addition, density functional theory (DFT) analysis was performed to explore the binding strength of Pd/NiFe-MOF/foam-Ni with CAP and the product and to obtain a deeper understanding of the mechanism of electrocatalytic hydrodechlorination of CAP. Finally, the stability of the Pd/NiFe-MOF/foam-Ni electrode was studied.

2. Materials and methods

2.1. Chemicals and materials

Iron nitrate ($Fe(NO_3)_3{\cdot}9H_2O$), palladium chloride ($PdCl_2$), and chloramphenicol (CAP) were purchased from Aladdin Biochemical Technology Co., Ltd, China. Nickel acetate tetrahydrate ($Ni(CH_3COOH)_2{\cdot}4H_2O$) and potassium 2,6-naphthalene dicarboxylate ($C_{12}H_6K_2O_4$) were supplied by Tianjin Damao Chemical Reagent Factory and Shanghai Yingxin Laboratory, respectively. Chromatography grade methanol used for high-performance liquid chromatography (HPLC)

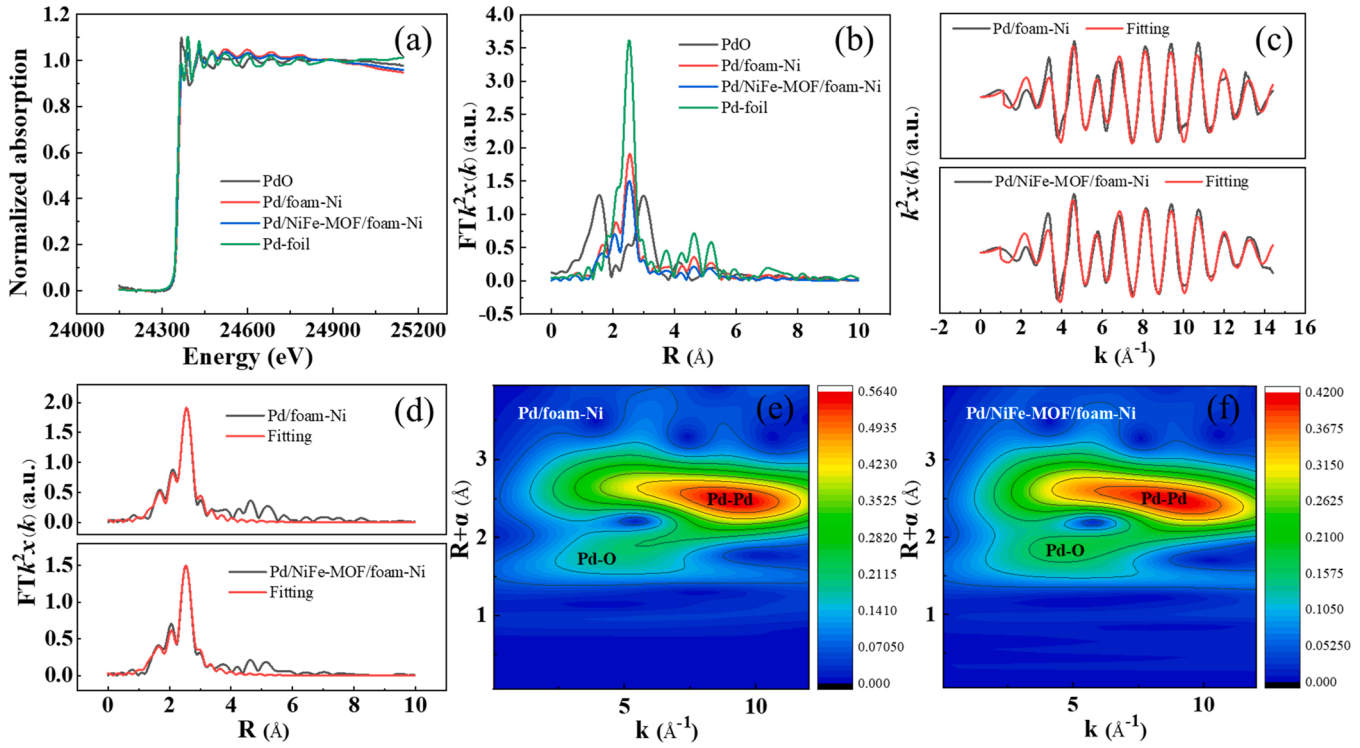

Fig. 4. (a) XANES of Pd K-edge; (b) Fourier transformation of the Pd K-edge EXAFS spectra; (c,d) Curve fitting of Pd K-edge data in K space and R space and (e,f) K-edge wavelet transform contour plots of Pd/foam-Ni and Pd/NiFe-MOF/foam-Ni.

measurement was provided by Tianjin North Tianyi Chemical Reagent Factory, China. Foam-Ni as the electrode substrate, was provided by Heze Tianyu Technology Development Co., Ltd. China.

2.2. Preparation of NiFe-MOF/foam-Ni electrode

Before fabrication, the foam-Ni (32 mm × 25 mm × 1 mm) was successively cleaned in acetone, 0.50 mol·L^{-1} H_2SO_4, and deionized water with ultrasonication. The supported solution of NiFe-MOF consisted of $Ni(CH_3COOH)_2{\cdot}4H_2O$, $Fe(NO_3)_3{\cdot}9H_2O$, and $C_{12}H_6K_2O_4$. Then, 120 mg of $Ni(CH_3COOH)_2{\cdot}4H_2O$ and 30 mg of $Fe(NO_3)_3{\cdot}9H_2O$ were added to a reaction kettle containing 15 mL of deionized water and mixed evenly. Foam-Ni was then placed into the reaction kettle, 150 mg of $C_{12}H_6K_2O_4$ was added, and the reactor was heated in a water bath at 333 K for 20 h. Finally, a NiFe-MOF/foam-Ni electrode was obtained and dried for use.

2.3. Preparation of Pd/NiFe-MOF/foam-Ni electrode

The preparation of the Pd/NiFe-MOF/foam-Ni electrode was achieved through an electrodeposition process. The NiFe-MOF/foam-Ni electrode was immersed as a cathode in a mixed solution of 1 mmol·L^{-1} $PdCl_2$ and 3 mmol·L^{-1} NaCl and then reacted at 313 K for 2 h under a constant current of 7 mA. Additionally, a platinum sheet was used as the anode in this process.

2.4. Electrochemical experiments

Electrocatalytic hydrodechlorination was carried out in a two-chamber reactor which we mentioned in our previous study [38]. The anode chamber and the cathode chamber are separated by a cation-exchange membrane (Nafion-117). Specifically, a 50 mL mixed solution of 0.05 mol·L^{-1} Na_2SO_4 and CAP was introduced into the cathode chamber, and 50 mL of 0.05 mol·L^{-1} Na_2SO_4 was introduced into the anode chamber. A Pd/NiFe-MOF/foam-Ni composite electrode was used as the cathode, and a platinum sheet was used as the anode. The constant current was 7 mA, and the temperature was 333 K.

2.5. Characterization

Scanning electron microscopy (SEM; FEI-Quanta FEG 250, USA) was performed to analyze the surface morphology of the electrode. A TecnaiG2 F30 transmission electron microscope (TEM; FEI Inc., USA) was used to characterize the particle size and subtle structure of the composite electrode. X-ray diffraction spectroscopy (XRD) was obtained by analyzing the crystal structure of the electrode with an X-ray diffractometer (DMAX-2500/PC, Japan). The surface of the composite electrode was analyzed by an X-ray photoelectron spectrometer (XPS; ESCALAB 250Xi, USA), and the characteristic peaks were fitted by Aventage 3.93 XPS software. Pd K-edge X-ray absorption near edge structure (XANES) and extended X-ray absorption fine structure (EXAFS) analyses were performed with Si (111) crystal monochromators at the BL14W Beam line at the Shanghai Synchrotron Radiation Facility (SSRF) (Shanghai, China). The detailed analysis method is in the Supplementary Information (Text S1). The adsorption capacity of the electrode substrate to Pd^{2+} was detected by inductively coupled plasma-optical emission spectrometer (ICP-OES; PerkinElmer Avio 200, USA). The electrochemical impedance spectroscopy (EIS). was performed in an electrochemical workstation (CHI660E, China) at frequencies from 10 MHz to 100 kHz to obtain the imaginary part (Z") and real part (Z′) of the electrical impedance at different frequencies. The cyclic voltammetry (CV) and chronopotential curve were also obtained by the CHI660E electrochemical workstation. A saturated calomel electrode was used as the reference electrode, and a platinum sheet (3 cm × 3 cm) was used as the counter electrode. Electron spin resonance spectroscopy (ESR; Bruker A300, Germany) was performed to determine the main active species in electrocatalytic hydrodechlorination. HPLC with a Shimazu LC-20AT and Inert Sustain C18 column (250 ×4.6 mm, 5 μm) was used to determine the concentration of CAP. The column temperature was 313 K. The mobile phase comprised a 40/60 mixture of methanol/water

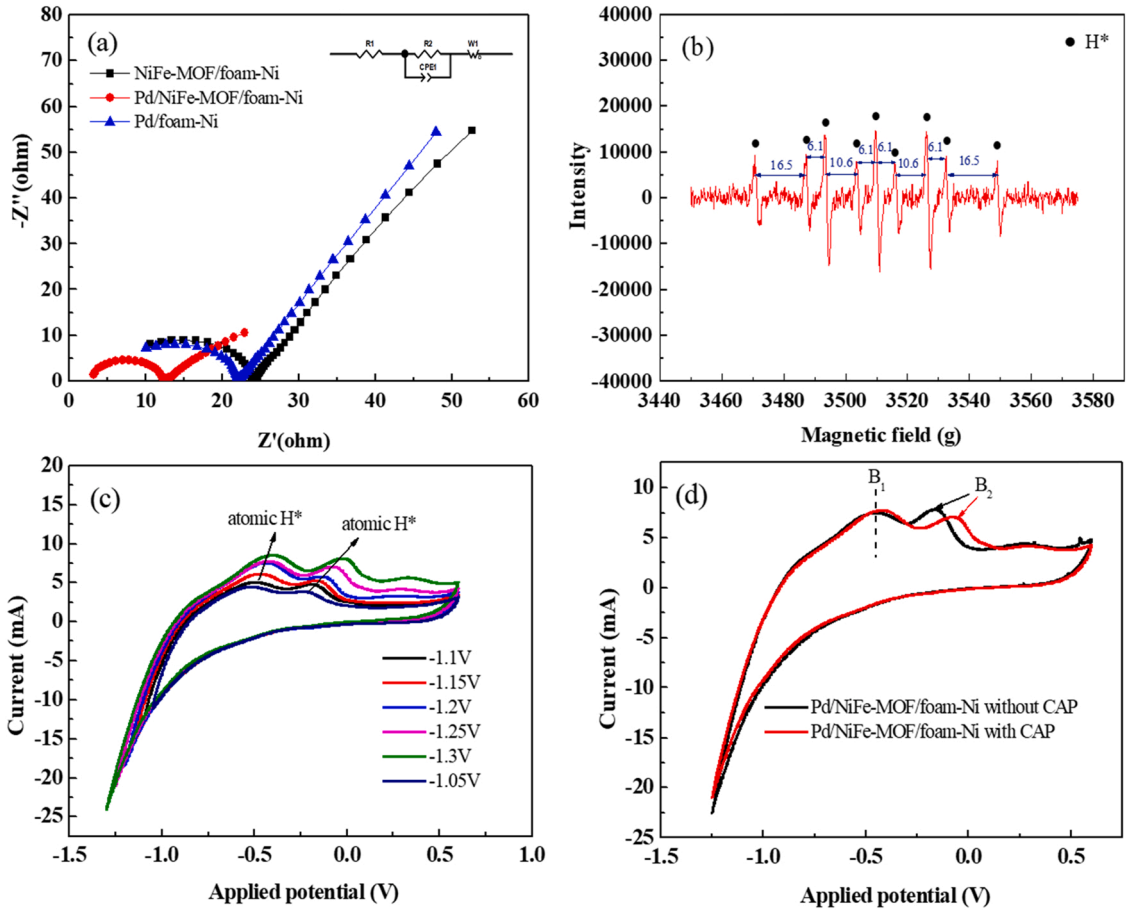

Fig. 5. Nyquist plots of NiFe-MOF/foam-Ni, Pd/foam-Ni, and Pd/NiFe-MOF/foam-Ni electrodes (a); The DMPO spin-trapping ESR spectra of Pd/NiFe-MOF/foam-Ni electrode (b); CVs of the Pd/NiFe-MOF/foam-Ni electrode with different CV starting potentials (c); CVs of Pd/NiFe-MOF/foam-Ni electrode with and without 35 mg·L^{-1} CAP (d) (T = 298 K, initial pH = 7.0, 35 mg·L^{-1} CAP).

at a flow rate of 1.00 mL·min^{-1}. A Shimazu LC-20AT UV detector was used, and the detection wavelength was 278 nm. The reaction pathway of CAP was detected and analyzed by liquid chromatography–mass spectrometry (LC-MS; Agilent 1290 UPLC/Agilent QTOF 6550, USA). The ecotoxicity of CAP and its reaction intermediates and products was evaluated by the ECOSAR 2.0 model.

2.6. DFT analyses

DFT calculations were completed in the Vienna Ab initio Software Package. The approximate energy functional Perdew–Burke–Ernzerhof (PBE) in the generalized gradient approximation (GGA) was determined to depict the correlation between electrons. The projected augmented wave (PAW) method could considerably reduce the number of plane waves necessary for atoms [39], and the cutoff energy was set to 400 eV. The 3 × 3 × 1 Monkhorst-Pack (MP) k-point grid sampling method was adopted to optimize the structure of NiFe-MOF/foam-Ni, Pd/foam-Ni, and Pd/NiFe-MOF/foam-Ni [40]. The force standard and convergence limit of atoms were 0.01 eV·Å^{-1} and 10^{-5} eV, respectively. A vacuum layer of 15 Å was used to eliminate the effect of periodic mirror images. The adsorption energy (E_{ads}) was calculated by:

$$E_{ads} = E_{tot} - \left(E_{adsorbate} + E_{catalyst}\right) \quad (1)$$

where E_{tot} represents the energy of the composite adsorbent, and $E_{adsorbate}$ and $E_{catalyst}$ are the adsorption energies of the adsorbate and catalyst surface, respectively.

The difference between the center position of the projected density of states (PDOS) corresponding to the *d*-states of the transition metal surface system and the Fermi energy level refers to the *d*-band center

$$\varepsilon_d = \frac{\int_{-\infty}^{\infty} n_d(\varepsilon)\varepsilon d\varepsilon}{\int_{-\infty}^{\infty} n_d(\varepsilon) d\varepsilon} \quad (2)$$

where ε_d represents the *d*-band center, $n_d(\varepsilon)$ refers to the *d*-state density, and ε is the electron energy level.

3. Results and discussion

3.1. Characterizations

The surface composition and structure of the foam-Ni, Pd/foam-Ni, NiFe-MOF/foam-Ni, and Pd/NiFe-MOF/foam-Ni electrodes are observed by SEM analysis. Foam-Ni possessed a three dimensional porous structure (Fig. S1a-b) and a large specific surface area (Fig. 1a), the dispersion of Pd on Pd/foam-Ni was not uniform (Fig. 1b). NiFe-MOF grown on foam-Ni was a kind of three-dimensional porous layer with high flexibility (Fig. S1c), and NiFe-MOF/foam-Ni had an excellent layered pore combination, which provided a large specific surface area and rich metal active sites for the deposition of Pd on the electrode (Fig. 1c). In addition, the structure and surface morphology of the Pd/NiFe-MOF/foam-Ni electrode were shown in Fig. 1d-e, the catalytic metal particles Pd dispersed uniformly on the prepared composite electrode (Fig. 1f). According to the high magnification microscope (Fig. S1d), the Pd on the surface of the Pd/NiFe-MOF/foam-Ni electrode presented a smooth spherical structure, which might be because the NiFe-MOF layer modified the growth environment of Pd on the composite electrode surface. This promoted the dispersion of Pd on the Pd/

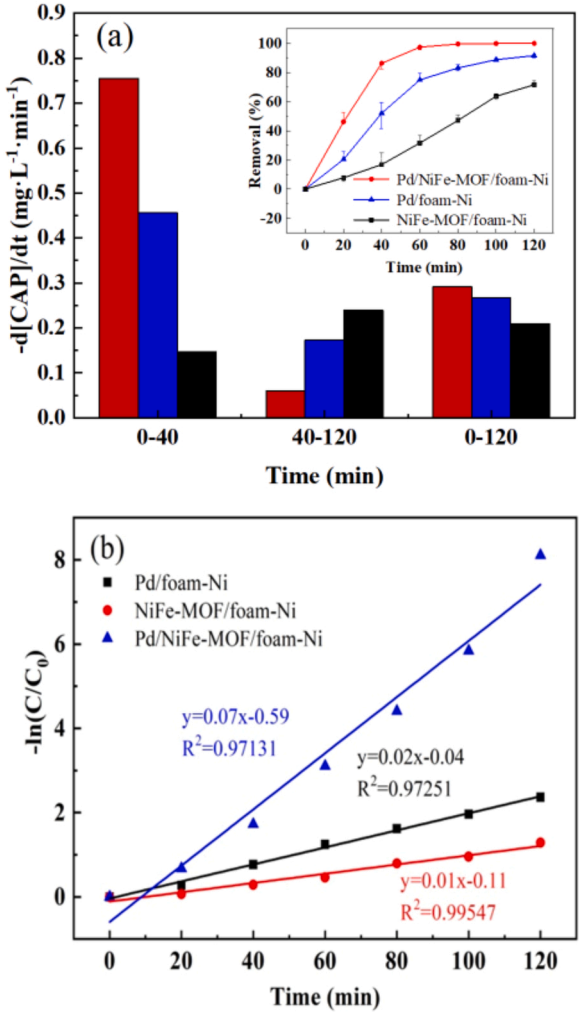

Fig. 6. Electrocatalytic hydrodechlorination of CAP at different electrodes (a) and corresponding linearized pseudo-first-order kinetic profiles (b) (T = 333 K, initial pH = 7.0, 35 mg·L^{-1} CAP).

NiFe-MOF/foam-Ni electrode. The corresponding energy dispersive spectroscopy (EDS) element diagram of Pd/NiFe-MOF/foam Ni showed C, O, N, Ni, Fe and Pd elements (Fig. 1g, Fig. S2).

According to the TEM images of the NiFe-MOF/foam-Ni and Pd/NiFe-MOF/foam-Ni electrodes, the NiFe-MOF/foam-Ni electrode shape was clear and smooth, with clear lattice fringes (Fig. S3). The catalytic metal Pd on the surface of the Pd/NiFe-MOF/foam-Ni electrode was granular and uniformly dispersed in a single shape, without agglomeration (Fig. 2a). According to the particle size distribution histogram, the Pd particles on the surface of the composite electrode were smaller than on Pd/foam-Ni (12 nm) reported in our previous work [21], and the average particle size was close to 3.17 nm (Fig. 2b) and was similar in different regions (Fig. S4). The results showed that the NiFe-MOF interlayer improved the agglomeration of Pd loaded on the composite electrode. From the high-resolution transmission electron microscopy (HRTEM) diagram (Fig. 2c), it is found that the lattice spacing of nanoparticles is 0.194 nm, which corresponds to the Pd (200) crystal plane [41]. The catalytic metal Pd was the main component and was evenly dispersed on the electrode surface in the TEM-EDS mapping (Fig. 2d). Moreover, the good uniformity and dispersion of Pd on the surface of the composite electrode increased the contact area with pollutants, which was conducive to the improvement of the electrocatalytic activity of the electrode [42].

Fig. 3a shows the XRD spectra of the obtained electrodes. For the Pd/

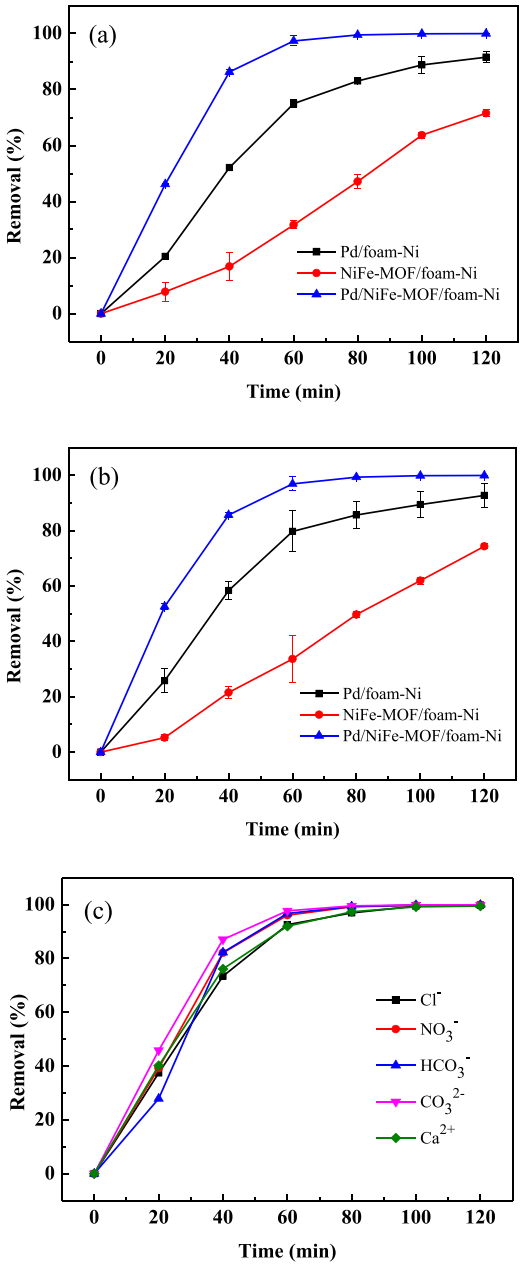

Fig. 7. Electrocatalytic hydrodechlorination of Pd/foam-Ni, NiFe-MOF/foam-Ni, and Pd/NiFe-MOF/foam-Ni at different sodium sulfite concentrations: (a) 1 mmol·L^{-1}, (b) 2 mmol·L^{-1}; (c) Effect of common ions on CAP electrocatalytic hydrodechlorination (T = 333 K, initial pH = 7.0, CAP=35 mg·L^{-1}).

NiFe-MOF/foam-Ni and NiFe-MOF/foam-Ni electrode, the characteristic peak at 9.32° proved the successful synthesis of NiFe-MOF (JCPDS No. 35–1677). The diffraction peaks at 39.78°, 46.32°, 67.30°, and 81.78° were attributed to the (111), (200), (220), and (311) planes of Pd (JCPDS No. 87–0643), respectively, which could be observed in the Pd/NiFe-MOF/foam-Ni and the Pd/foam-Ni electrode. After deposition of Pd, the crystallinity of NiFe-MOF was well preserved in the Pd/NiFe-MOF/foam-Ni electrode. In addition, the sharp peaks at 2θ of 44.24°, 51.66°, and 76.02° correspond to the (111), (200) and (220) crystal faces of Ni (JCPDS No. 89–7128), respectively. Then, the crystal structure of Pd/NiFe-MOF/foam-Ni electrode remained intact before and after the hydrodechlorination reaction (Fig. S5).

The elemental composition and chemical valence of the surface layer of the materials were investigated by XPS. The peak at 284.78 eV proved the existence of C-C. The peaks at 286.08 eV and 287.48 eV

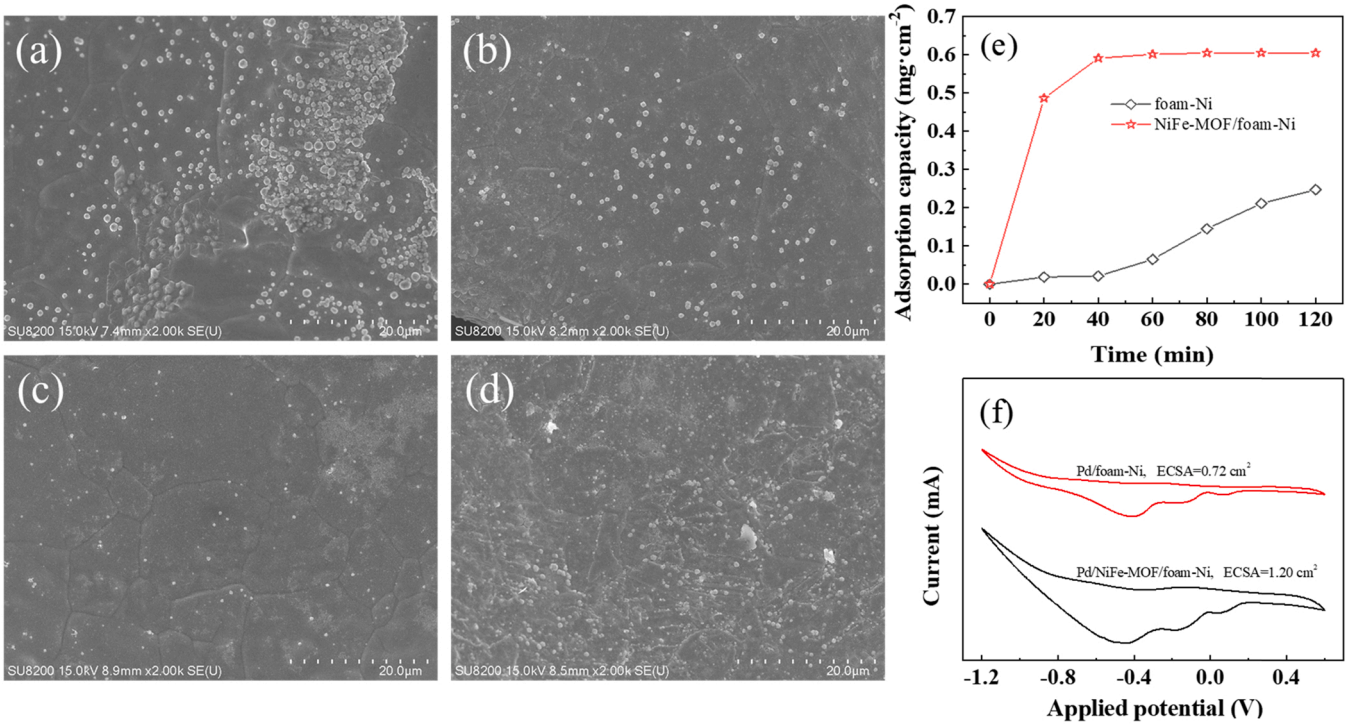

Fig. 8. SEM images of (a) Pd/foam-Ni and (b) Pd/NiFe-MOF/foam-Ni with Pd electrodeposition time of 2 min; The growth state of Pd adsorbed on the (c) foam-Ni and (d) NiFe-MOF/foam-Ni electrode substrate (in NaCl electrolyte and with electric field); (e) The adsorption capacity of foam-Ni and NiFe-MOF/foam-Ni to Pd^{2+} at different reaction times; (f) CVs of the Pd/foam-Ni and Pd/NiFe-MOF/foam-Ni electrode with a scanning rate of 20 mV·s^{-1} in 0.10 mol·L^{-1} Na_2SO_4 solution (T = 298 K, initial pH = 7.0).

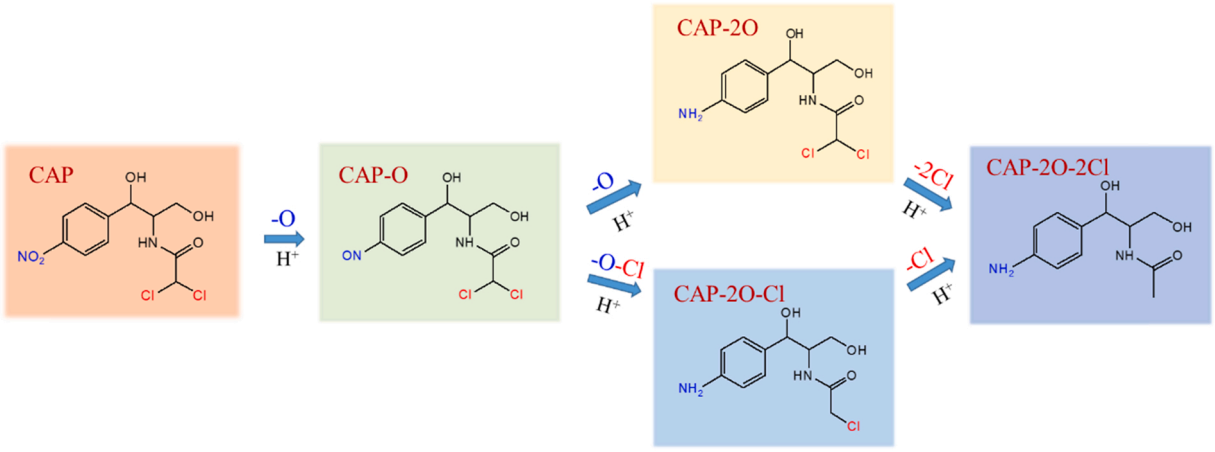

Fig. 9. Proposed pathway of CAP removal by Pd/NiFe-MOF/foam-Ni electrode (T = 333 K, initial pH = 7.0, 35 mg·L^{-1} CAP).

corresponded to the presence of C-O and C-N in the Pd/NiFe-MOF/foam-Ni electrode, respectively (Fig. S6a). Fig. 3b-d shows the XPS spectra of Pd 3d, Ni 2p, and Fe 2p. The main characteristic peaks corresponded to 334.57 eV and 339.85 eV binding energies, which were ascribed to Pd^0 $3d_{5/2}$ and Pd^0 $3d_{3/2}$ of zero-valent metal Pd, respectively, while the satellite peaks of 342.17 eV and 337.03 eV corresponded to Pd^{2+} in the electrode. This might be because a part of the zero-valent Pd on the electrode surface was oxidized. Especially, both the Pd $3d_{5/2}$ and Pd $3d_{3/2}$ peaks of the Pd/NiFe-MOF/foam-Ni electrode exhibited a negative shift of 0.5 eV compared to the Pd/foam-Ni electrode. The result showed that a relatively strong interfacial interaction was formed between NiFe-MOF and Pd, and electrons were transferred from the interlayer to the Pd nanoparticles, resulting in an electron-rich Pd [43,44]. The binding energy of the Ni 2p orbital at 873.00 eV and 855.60 eV of the prepared electrode was attributed to the divalent oxidation state of Ni. The spin orbitals of the Fe 2p orbital at 725.28 eV and 711.48 eV indicated that Fe mainly exists in the form of trivalent oxidation state in Pd/NiFe-MOF/foam-Ni. Besides, the signals of Pd, Ni and Fe on the used Pd/NiFe-MOF/foam-Ni electrode did not change significantly, which again proved that the structure of Pd/NiFe-MOF/foam-Ni remained stable (Fig. S6b-d).

In order to obtain the detailed electronic structure and coordination environment of Pd, we recorded the Pd K-edge XANES and EXAFS spectra [45]. The absorption edges of both were slightly to the right of Pd foil in XANES, indicating that the valence state of the two electrodes were little higher than Pd foil. Notably, the Pd/NiFe-MOF/foam-Ni is less oxidized (Fig. 4a). The EXAFS spectrum showed a main peak at 2.74 Å (Fig. 4b). Combined with the fitting curve (Fig. 4c-d, Fig. S7) of

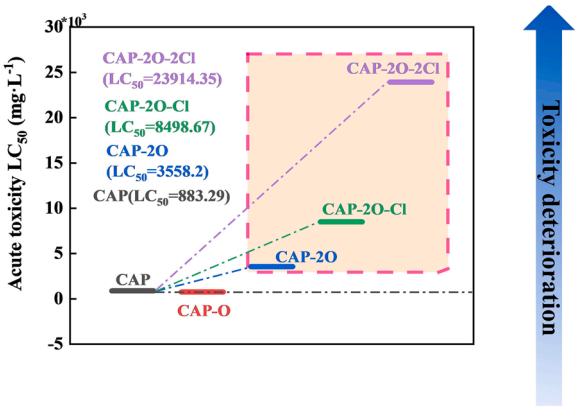

Fig. 10. The toxicity evolution of reaction products evaluated by ECOSAR predictive model.

quantitative coordination analysis of Pd atoms and detailed data (Table S1), it proved that Pd-Pd was the main coordination environment. Interestingly, the peak intensity of Pd/NiFe-MOF/foam-Ni was a little lower than that of Pd/foam-Ni, and the coordination number was a little smaller, indicating the particle size of Pd on Pd/NiFe-MOF/foam-Ni was smaller [46], which corresponded to the TEM results. The contour map of wavelet transform further proved that Pd-Pd was the main coordination bond and only a small amount of Pd particles were oxidized on the electrode surface (Fig. e-f).

3.2. Electrochemical properties

The electrochemical performance of the Pd/NiFe-MOF/foam-Ni composite electrode was investigated at 298 K in 0.1 mol·L^{-1} Na_2SO_4 solution by EIS. Zeview2 software was used to simulate the equivalent circuit diagrams. Fig. 5a shows the Nyquist diagrams of the three electrodes. The equivalent circuit fitting model of the electrode was R (RC) W. The high-frequency region is controlled by the electrode reaction kinetics (charge transfer process) [47], and the diameter of the semicircle represents the charge transfer resistance (Rct) of the electrode [48]. The charge transfer resistance values of the Pd/NiFe-MOF/foam-Ni, NiFe-MOF/foam-Ni, and Pd/foam-Ni electrodes were 11.55 Ω, 18.15 Ω, and 17.59 Ω, respectively. Among them, the Rct value of the Pd/NiFe-MOF/foam-Ni electrode was the smallest, indicating the best electrical conductivity. The results showed that the synergistic effect of the NiFe-MOF layer and Pd in the Pd/NiFe-MOF/foam-Ni electrode improved the electron transfer capability at the electrode/electrolyte interface and accelerated the electrode reaction kinetics process [49].

3.3. Identification of active hydrogen species for electrocatalytic hydrodechlorination

The main active substances in the electrocatalytic hydrodechlorination of CAP were determined by ESR (Fig. 5b). Among them, the ESR signal peak on the Pd/NiFe-MOF/foam-Ni electrode was visible, showing a strong ninefold characteristic peak of dimethyl pyridine N-oxide (DMPO)-H. Therefore, this confirmed that H* was indeed produced and involved in the electrocatalytic hydrodechlorination process.

To study the evolution of H* on the Pd/NiFe-MOF/foam-Ni electrode, the cyclic voltammetry (CV) was performed at a scanning rate of 50 mV·s^{-1} from − 1.30 V to − 1.05 V in 0.1 mol·L^{-1} Na_2SO_4 solution [50]. Fig. 5c shows two oxidation peaks at − 0.80 ~ − 0.40 V and − 0.20 ~ − 0.00 V potentials in positive scans [51], respectively. According to the literature [51], these two oxidation peaks might be related to the consumption of H* on the polycrystalline Pd (111) and (200) planes. No H_2 oxidation peak was detected in a range of CV scans.

Subsequently, we compared the cyclic voltammograms of Pd/foam-Ni and Pd/NiFe-MOF/foam-Ni in the presence and absence of CAP under starting potentials of − 1.20 V and termination potential at 0.60 V (Fig. S8). Interestingly, Fig. 5d shows that the peaks of − 0.80 ~

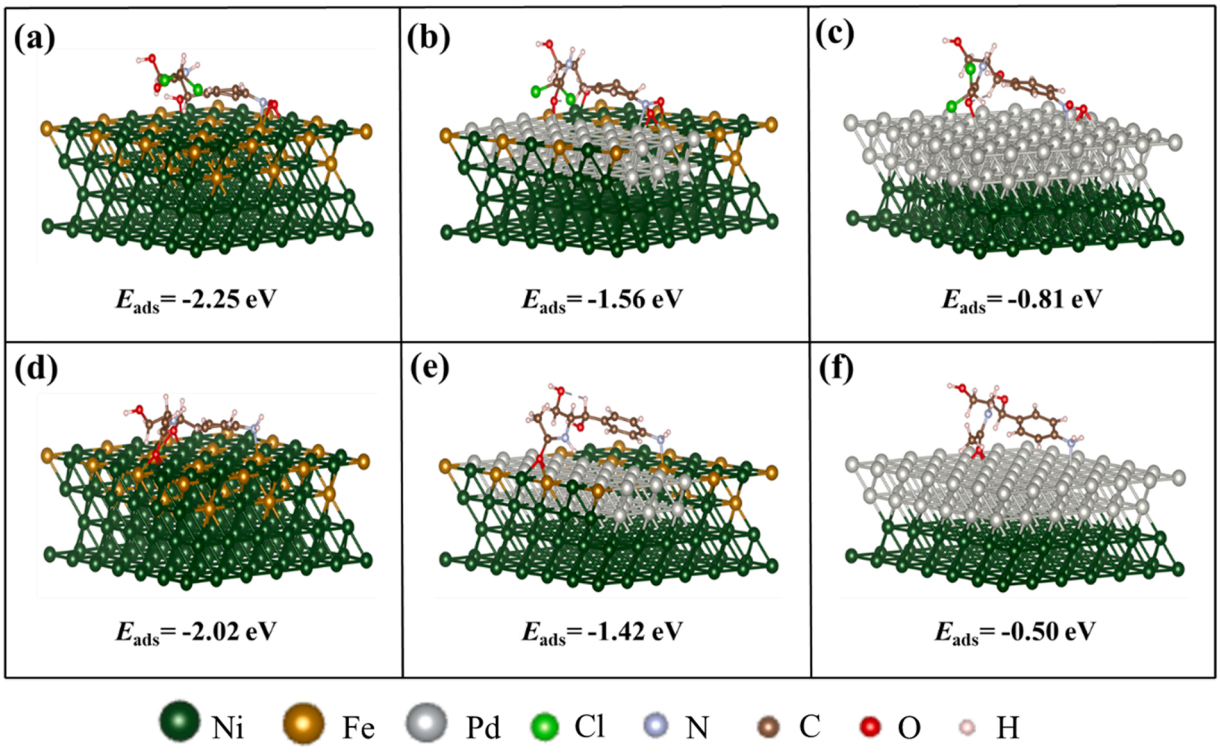

Fig. 11. DFT analyses on the adsorption configurations and energies of (a, d) CAP, CAP-2 O-2Cl on NiFe-MOF/foam-Ni, (b, e) CAP, CAP-2 O-2Cl on Pd/NiFe-MOF/foam-Ni, and (c, f) CAP, CAP-2 O-2Cl on Pd/foam-Ni, respectively.

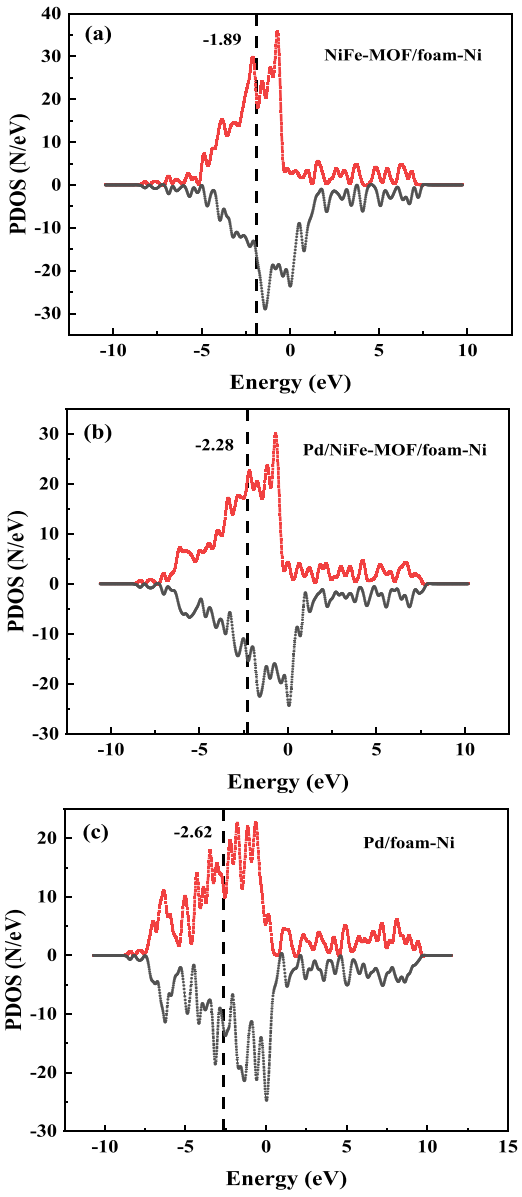

Fig. 12. *d*-Projected density of states (*d*-PDOS) in NiFe-MOF/foam-Ni (a), Pd/NiFe-MOF/foam-Ni (b), and Pd/foam-Ni (c). Black dotted line: Position of the *d* band center (ε_d).

− 0.40 V remained stable, while the peak intensities of − 0.20 ~ − 0.00 V were lower after the addition of CAP. These results indicated that the adsorbent H* at the peak of − 0.20 ~ − 0.00 V was the dominant active hydrogen species [49].

3.4. Electrocatalytic hydrodechlorination of CAP using different electrodes

To study the electrocatalytic hydrodechlorination efficiency of different electrodes on CAP, a range of CAP concentrations (20, 30, 35, 40, 50 mg·L^{-1}) was selected and studied in specific experiments (Fig. S9). The removal efficiency of the composite electrode for all concentrations of CAP reached 100% when the reaction time was 2 h. However, the removal efficiency of the Pd/NiFe-MOF/foam-Ni electrode for CAP increased with increasing initial concentration of CAP within 0–80 min and then decreased. When the initial concentration of CAP was 35 mg·L^{-1}, the Pd/NiFe-MOF/foam-Ni electrode had the best performance. The Pd/NiFe-MOF/foam-Ni composite electrode could remove CAP at a relatively high rate within 0–40 min and completely remove it within 120 min. CAP was only removed by 90.62% and 72.41% by using the Pd/foam-Ni and NiFe-MOF/foam-Ni electrodes, respectively (Fig. 6a). The CAP removal kinetics was studied using the pseudo-first-order kinetics model (Fig. 6b).

$$\ln\left(\frac{C}{C_0}\right) = -k_{obs}t \quad (3)$$

where C (mg·L^{-1}) and C_0 (mg·L^{-1}) represent the concentration at time t and initial concentrations of CAP, respectively; k_{obs} (min^{-1}) is the reaction rate constant; and t (min) is the reaction time.

The reaction rate constants of CAP by Pd/foam-Ni, NiFe-MOF/foam-Ni, and Pd/NiFe-MOF/foam-Ni in the electrocatalytic hydrodechlorination system of CAP were 0.02 min^{-1}, 0.01 min^{-1}, and 0.07 min^{-1}, respectively. The k_{obs} of the Pd/NiFe-MOF/foam-Ni electrode was the highest, indicating that it had better electrocatalytic performance, which might be attributed to the good porosity and large specific surface area of the NiFe-MOF interlayer.

3.5. Influence of sulfite and common ions on the electrocatalytic performance of electrodes

Supported metal catalysts are sensitive to sulfur species and are easily deactivated by sulfur concentration, exposure time, and chemical form [52–54]. Therefore, the resistance of electrodes to sulfites was investigated in this paper. As shown in Fig. 7a-b, the electrocatalytic activity of the Pd/foam-Ni, NiFe-MOF/foam-Ni, and Pd/NiFe-MOF/foam-Ni electrodes was almost unaffected in the presence of 1 mmol·L^{-1} and 2 mmol·L^{-1} sodium sulfite. The Pd/NiFe-MOF/foam-Ni electrode could still completely remove CAP within 120 min. The removal efficiencies of CAP by Pd/foam-Ni and NiFe-MOF/foam-Ni had no obvious change. Therefore, the Pd/foam-Ni, NiFe-MOF/foam-Ni, and Pd/NiFe-MOF/foam-Ni electrodes had good resistance to sulfites.

In this paper, the effects of inorganic anions (Cl^-, NO_3^-, HCO_3^-, CO_3^{2-}) and cations (Ca^{2+}) at a concentration of 2 mmol·L^{-1} on the electrocatalytic hydrodechlorination of CAP by a Pd/NiFe-MOF/foam-Ni electrode were further studied (Fig. 7c). The influence of Cl^-, NO_3^-, HCO_3^-, CO_3^{2-} and Ca^{2+} on the electrocatalytic hydrodechlorination efficiency of CAP at the electrode was almost negligible. Even in the presence of these conventional cations and anions, the removal of CAP by the electrode could still reach more than 99% after 120 min. The experimental results showed that the electrocatalytic hydrodechlorination system of CAP with the Pd/NiFe-MOF/foam-Ni electrode was relatively stable and minimally affected by the external environment.

3.6. Discussion

In order to further explore the possible factors for the high catalytic activity of Pd/NiFe-MOF/foam-Ni electrode, in addition to the results provided by the above XPS (Fig. 3b), it was proved that the interface action between NiFe-MOF and Pd regulated its electronic structure and increased the electron density of Pd [55–57]. We also need to consider the effects of other aspects.

By observing the SEM images of Pd/NiFe-MOF/foam-Ni and Pd/foam-Ni electrodes with Pd deposition time of 2 min (Fig. 8a-b, Text S2), it could be seen that Pd particles on Pd/foam-Ni were agglomerated, while Pd on Pd/NiFe-MOF/foam-Ni electrodes were uniformly dispersed. This may be because NiFe-MOF preferentially adsorbed palladium ions, anchored nucleation sites, and formed abundant Pd nucleus, thus forming Pd particles with smaller particle sizes [58–60]. In addition, we observed the growth state of Pd absorbed on the electrode substrate (in NaCl electrolyte and with electric field) (Fig. 8c-d, Text S3) [61]. The results showed that the Pd particles on the foam-Ni grew slowly and were few in number. However, Pd particles on the NiFe-MOF

continued to grow normally along the adsorbed Pd sites, which further verified that the introduction of NiFe-MOF increased the nucleation sites of Pd and thus improved the electrocatalytic effect [62–64].

In order to further prove the adsorption of NiFe-MOF to Pd^{2+}, we used ICP-OES to detect the adsorption capacity of foam-Ni and NiFe-MOF to Pd^{2+} (Fig. 8e, Text S4). The adsorption capacity of NiFe-MOF to Pd^{2+} increased rapidly within 20 min, and then increased at a slower rate, reaching a saturated adsorption capacity of 0.61 $mg{\cdot}cm^{-2}$ at 80 min. However, the adsorption capacity of foam-Ni to Pd^{2+} had been increasing slowly, reaching only 0.25 $mg{\cdot}cm^{-2}$ at 120 min. It could be seen that NiFe-MOF had good adsorption performance for Pd^{2+}, which could be attributed to its high specific surface area [28].

Significantly, the introduction of NiFe-MOF interlayer improves its electrochemical active surface area (ECSA) [65] and increases the Pd nucleation sites [66]. To confirm this hypothesis, the ECSAs of the Pd/foam-Ni and Pd/NiFe-MOF/foam-Ni electrodes were calculated. According to the reduction peak area of PdO in the CV curve, the ECSA could be calculated by methods in the literature [67,68].

According to the CV curve, the ECSAs of the Pd/foam-Ni and Pd/NiFe-MOF/foam-Ni electrodes were 0.72 cm^2 and 1.20 cm^2, respectively (Fig. 8f). It could be concluded that the ECSA value of the Pd/NiFe-MOF/foam-Ni composite electrode was large, and the active sites were the most abundant. The experimental results indicated that the large specific surface area of the NiFe-MOF interlayer provided an excellent growth environment for Pd loading. The synergistic effect of the NiFe-MOF interlayer and catalytic metal Pd improved the electrocatalytic performance of the electrode.

3.7. Reaction pathway and ecotoxicity assessment

The reaction intermediates and products of CAP by the Pd/NiFe-MOF/foam-Ni electrode were identified to elucidate the pathway of CAP removal. The CAP reaction products in the treatment process were investigated by LC-MS analysis (Fig. S10). According to the results of LC-MS analysis, the proposed pathway of electrocatalytic hydrodechlorination of CAP by Pd/NiFe-MOF/foam-Ni electrode is shown in Fig. 9. First, the chromatographic peak of CAP with *m/z* 323 gradually disappears (Fig. S10a). Subsequently, an O atom on the nitro group ($-NO_2$) is reduced to obtain the first intermediate CAP-O ($C_{11}H_{12}Cl_2N_2O_4$) with *m/z* 307 (Fig. S10b). Then, the formation of product CAP-2 O ($C_{11}H_{14}Cl_2N_2O_3$) of *m/z* 293 shows that another O atom on the nitro group ($-NO_2$) is also reduced, and $-NO_2$ is completely reduced to $-NH_2$ (Fig. S10b). With the increase of reaction time, one Cl atom is removed by dechlorination to yield the product CAP-2 O-Cl ($C_{11}H_{15}ClN_2O_3$) inferred by the detection of a fragment with *m/z* 259 (Fig. S10c). Finally, a fragment with *m/z* 223 indicates that another Cl atom is also removed via dechlorination to yield the final product CAP-2 O-2Cl ($C_{11}H_{16}N_2O_3$) (Fig. S10d) [69,70].

Furthermore, the ecotoxicity of CAP and reaction intermediates and products was assessed using the ECOSAR model. The acute toxicity of these compounds was evaluated considering fish and daphnia as indicators. Table S2 summarizes the detailed toxicity values of CAP and reaction intermediates and products. Generally, a compound may belong to multiple chemical classes based on the ECOTOX database accepted by ECOSAR [71]. The evaluation targets were uniformly attributed to the chemical class of benzyl alcohols, and the toxicity evolution of CAP and its products was plotted, as shown in Fig. 10. The acute toxicity of intermediate products CAP-2 O, CAP-2 O-Cl and final product CAP-2 O-2Cl for fish decreased by 4 times (833.29 $mg{\cdot}L^{-1}$ for CAP and 3558.2 $mg{\cdot}L^{-1}$ for CAP-2 O), 10 times (8498.67 $mg{\cdot}L^{-1}$ for CAP-2 O-Cl) and 30 times (23914.35 $mg{\cdot}L^{-1}$ for CAP-2 O-2Cl), respectively. The results showed that the ecotoxicity of CAP decreased significantly with the progress of electrocatalytic hydrochlorination, and even the LC_{50} of some products exceeded the water solubility of them, which would not cause harm to the ecosystem.

3.8. Stability of Pd/NiFe-MOF/foam-Ni electrode

By investigating the stability of the prepared composite electrode, the performance and application potential of the electrode were further studied. In this study, the reusability of the composite electrode within 6 cycles was explored (Fig. S11a). After 6 cycles, the removal efficiency of CAP on the composite electrode could still reach 99.12%, indicating that the composite electrode had good stability in 6 cycles. In addition, the stability of the Pd/NiFe-MOF/foam-Ni electrode in 0.1 $mol{\cdot}L^{-1}$ Na_2SO_4 solution was tested at a constant current density (Fig. S11b). The current density increased from 5 mA to the optimal reaction current of 7 mA. The potential remained almost unchanged during each 3600 s test cycle [72] and remained stable throughout the entire 7200 s test cycle, proving its stability.

3.9. Mechanism study

To examine the influence of the introduction of NiFe-MOF in the intermediate layer, DFT analysis was used to compare the bonding strength of CAP and the hydrodechlorination product (CAP-2 O-2Cl) with that of the catalyst. By calculating five different adsorption configurations of CAP, it was found that the configuration of the CAP benzene ring parallel to the catalyst was the most stable, with an adsorption energy of − 0.85 eV (Fig. S12). Fig. 11 shows the optimized adsorption configuration and lists the corresponding adsorption energies. The results showed that CAP and CAP-2 O-2Cl had the strongest adsorption capacity for NiFe-MOF/foam-Ni, followed by Pd/NiFe-MOF/foam-Ni, and Pd/foam-Ni in this order. Further, combining the DFT analysis and the electrocatalytic hydrodechlorination performance of the electrodes, we found that NiFe-MOF/foam-Ni, which was strongly combined with CAP, did not obtain the highest activity (Fig. 6). On the other hand, Pd/foam-Ni, whose interaction with CAP-2 O-2Cl was weaker, also had lower activity. The adsorption of CAP and the desorption of CAP-2 O-2Cl had an important influence on the performance of electrocatalytic hydrodechlorination. Too strong adsorption was conducive to the adsorption of CAP, but not good for the desorption of CAP-2 O-2Cl, resulting in the reduction of the active centers. However, weak adsorption had a negative effect on the capture of CAP, although it was beneficial to the desorption of CAP-2 O-2Cl. In general, the best catalyst should have a medium adsorption capacity to balance the adsorption of CAP and the desorption of CAP-2 O-2Cl [73]. Therefore, Pd/NiFe-MOF/foam-Ni was the most optimum catalytic material and thus delivered the largest contribution to electrocatalytic hydrodechlorination.

Fig. 12a-c shows the *d*-projected density of states (*d*-PDOS) of NiFe-MOF/foam-Ni, Pd/NiFe-MOF/foam-Ni, and Pd/foam-Ni. The *d* band centers of the three catalysts were − 1.89, − 2.28, and − 2.62 eV, respectively. We believed that the *d* band center could describe the adsorption capacity of the catalyst in the reaction. The closer the *d* band center was to 0 eV, the greater the adsorption energy. Since the *d* band center of Pd/NiFe-MOF/foam-Ni was in the middle, it proved again that it was the best catalytic material, and it also revealed that the *d* band center should be a potential indicator of electrocatalytic hydrodechlorination performance [74–76].

4. Conclusions

In conclusion, a Pd/NiFe-MOF/foam-Ni composite electrode was successfully prepared. The Pd/NiFe-MOF/foam-Ni electrode had good electrocatalytic hydrodechlorination performance. CAP was completely removed within 120 min. After 6 cycles, it was found that the electrode was stable, and the removal of CAP could reach 99.1%. The NiFe-MOF interlayer was introduced to obtain a Pd catalyst with small particle size and good dispersion, which improved the catalytic activity of the metal Pd on the composite electrode surface to a certain extent. In addition, electrons were transferred from NiFe-MOF interlayer to Pd

nanoparticles to form electron-rich Pd, which accelerated the process of electrocatalytic hydrochlorination. The Pd on Pd/NiFe-MOF/foam-Ni electrode was slightly oxidized and Pd-Pd was the main coordination environment by XAFS analysis. The effect of sulfite and common ions on the electrocatalytic hydrodechlorination of the Pd/NiFe-MOF/foam-Ni electrode was almost negligible. It was suggested that the reaction intermediates and products of the electrocatalytic hydrodechlorination of CAP were mainly CAP-O, CAP-2 O, CAP-2 O-Cl, and CAP-2 O-2Cl. The reaction intermediates and products of CAP will not cause damage to the ecosystem according to the ECOSAR assessment data. Pd/NiFe-MOF/foam-Ni had a moderate binding energy between molecules, and the *d* band center could be confirmed via DFT calculations. The Pd/NiFe-MOF/foam-Ni electrode exhibited excellent stability and had promising prospects in the electrocatalytic hydrodechlorination treatment of chlorinated PPCPs.

CRediT authorship contribution statement

Junjing Li: Conceptualization, Methodology; Shumin Ma: Data curation, Writing – original draft preparation;Ziyan Qi: Data curation, Formal analysis; Jing Ding: Formal analysis;Menghua Yin: Formal analysis, Bin Zhao: Formal analysis;Zhaohui Zhang: Formal analysis;Yu Wang: Formal analysis;Hongwei Zhang: Supervision;Liang Wang: Supervision;Dionysios D. Dionysiou: Writing – review & editing, Supervision.

Declaration of Competing Interest

The authors declare that they have no known competing financial interests or personal relationships that could have appeared to influence the work reported in this paper.

Data Availability

No data was used for the research described in the article.

Acknowledgments

This work was kindly supported by China Postdoctoral Science Foundation (2020T130470, 2018M641656), Open Project of State Key Laboratory of Urban Water Resource and Environment (QG202231), Scientific Research Plan Project of Tianjin Municipal Education Commission (2017KJ077), National Natural Science Foundation of China (51508385, 51978465), Tianjin Science and Technology Foundation (19JCZDJC39800), TGU Grant for Fiber Studies (TGF-21-B3).

Appendix A. Supporting information

Supplementary data associated with this article can be found in the online version at doi:10.1016/j.apcatb.2022.122076.

References

[1] Z.X. Zheng, I.M.C. Lo, Fabrication of MoS_2@BL-$BiVO_4$ photoanode with promoted charge separation for photoelectrochemical sewage treatment to simultaneously degrade PPCPs, disinfect *E. coli*, and produce H_2: Performance, mechanisms, and influence factors, Appl. Catal. B Environ. 299 (2021), 120636, https://doi.org/10.1016/j.apcatb.2021.120636.

[2] D. Liu, K. Song, G.J. Xie, L. Li, MBR-UV/Cl_2 system in treating polluted surface water with typical PPCP contamination, Sci. Rep. 10 (2020) 1–8, https://doi.org/10.1038/s41598-020-65845-w.

[3] Y.N. Xing, X.J. Chen, X. Chen, J. Zhuang, Colloid-mediated transport of pharmaceutical and personal care products through porous media, Sci. Rep. 6 (2016) 1–10, https://doi.org/10.1038/srep35407.

[4] M.M. Pan, T. Lyu, L.M. Zhan, V. Matamoros, I. Angelidaki, M. Cooper, G. Pan, Mitigating antibiotic pollution using cyanobacteria: Removal efficiency, pathways and metabolism, Water Res. 190 (2021), 116735, https://doi.org/10.1016/j.watres.2020.116735.

[5] X.Y. Xin, G. Huang, B.Y. Zhang, Review of aquatic toxicity of pharmaceuticals and personal care products to algae, J. Hazard. Mater. 410 (2021), 124619, https://doi.org/10.1016/j.jhazmat.2020.124619.

[6] H.Y. Chen, L.J. Jing, Y.G. Teng, J.S. Wang, Characterization of antibiotics in a large-scale river system of China: occurrence pattern, spatiotemporal distribution and environmental risks, Sci. Total Environ. 618 (2018) 409–418, https://doi.org/10.1016/j.scitotenv.2017.11.054.

[7] L.L. Xiao, J.J. Li, E. Lichtfouse, Z.K. Li, Q. Wang, F.H. Liu, Augmentation of chloramphenicol degradation by Geobacter-based biocatalysis and electric field, J. Hazard. Mater. 410 (2021), 124977, https://doi.org/10.1016/j.jhazmat.2020.124977.

[8] X. Jin, D.D. Wu, Z.Y. Chen, C. Wang, C. Liu, C. Gu, Surface catalyzed hydrolysis of chloramphenicol by montmorillonite under limited surface moisture conditions, Sci. Total Environ. 770 (2021), 144843, https://doi.org/10.1016/j.scitotenv.2020.144843.

[9] F. Suanon, Q. Sun, M.Y. Li, X. Cai, Y.C. Zhang, Y.J. Yan, C.P. Yu, Application of nanoscale zero valent iron and iron powder during sludge anaerobic digestion: Impact on methane yield and pharmaceutical and personal care products degradation, J. Hazard. Mater. 321 (2017) 47–53, https://doi.org/10.1016/j.jhazmat.2016.08.076.

[10] H. Zhao, Z. Cao, X. Liu, Y. Zhan, J. Zhang, X. Xiao, Y. Yang, J.L. Zhou, J. Xu, Seasonal variation, flux estimation, and source analysis of dissolved emerging organic contaminants in the Yangtze Estuary, China, Mar. Pollut. Bull. 125 (2017) 208–215, https://doi.org/10.1016/j.marpolbul.2017.08.034.

[11] W.L. Chen, Y.S. Ling, D.J.H. Lee, X.Q. Lin, Z.Y. Chen, H.T. Liao, Targeted profiling of chlorinated transformation products and the parent micropollutants in the aquatic environment: a comparison between two coastal cities, Chemosphere 242 (2020), 125268, https://doi.org/10.1016/j.chemosphere.2019.125268.

[12] W.L. Chen, J.Y. Cheng, X.Q. Lin, Systematic screening and identification of the chlorinated transformation products of aromatic pharmaceuticals and personal care products using high-resolution mass spectrometry, Sci. Total Environ. 637 (2018) 253–263, https://doi.org/10.1016/j.scitotenv.2018.05.011.

[13] D. Muir, D. Simmons, X.W. Wang, T. Peart, M. Villella, J. Miller, J. Sherry, Bioaccumulation of pharmaceuticals and personal care product chemicals in fish exposed to wastewater effluent in an urban wetland, Sci. Rep. 7 (2017) 1–11, https://doi.org/10.1038/s41598-017-15462-x.

[14] H.L. Qian, G.J. Yu, Q.D. Hou, Y.F. Nie, C.Y.L. Bai, X.Y. Bai, H.Z. Wang, M.T. Ju, Ingenious control of adsorbed oxygen species to construct dual reaction centers ZnO@FePc photo-Fenton catalyst with high-speed electron transmission channel for PPCPs degradation, Appl. Catal. B Environ. 291 (2021), 120064, https://doi.org/10.1016/j.apcatb.2021.120064.

[15] A. Kumar, M. Khan, J.H. He, I.M.C. Lo, Visible-light-driven magnetically recyclable terephthalic acid functionalized g-C_3N_4/TiO_2 heterojunction nanophotocatalyst for enhanced degradation of PPCPs, Appl. Catal. B Environ. 270 (2020), 118898, https://doi.org/10.1016/j.apcatb.2020.118898.

[16] Z. Cao, H. Li, G.V. Lowry, X.Y. Shi, X.C. Pan, X.H. Xu, G. Henkelman, J. Xu, Unveiling the role of sulfur in rapid defluorination of florfenicol by sulfidized nanoscale zero-valent iron in water under ambient conditions, Environ. Sci. Technol. 55 (2021) 2628–2638, https://doi.org/10.1021/acs.est.0c07319.

[17] J. Xu, H. Li, G.V. Lowry, Sulfidized nanoscale zero-valent iron: Tuning the properties of this complex material for efficient groundwater remediation, Acc. Mater. Res. 2 (2021) 420–431, https://doi.org/10.1021/accountsmr.1c00037.

[18] Z. Cao, H. Li, X.H. Xu, J. Xu, Correlating surface chemistry and hydrophobicity of sulfidized nanoscale zerovalent iron with its reactivity and selectivity for denitration and dechlorination, Chem. Eng. J. 394 (2020), 124876, https://doi.org/10.1016/j.cej.2020.124876.

[19] Z.R. Sun, X.F. Wei, H. Zhang, X. Hu, Dechlorination of pentachlorophenol (PCP) in aqueous solution on novel Pd-loaded electrode modified with PPy-SDBS composite film, Environ. Sci. Pollut. Res. 22 (2015) 3828–3837, https://doi.org/10.1007/s11356-014-3641-x.

[20] X.Z. Song, Q. Shi, H. Wang, S.L. Liu, C. Tai, Z.Y. Bian, Preparation of Pd-Fe/graphene catalysts by photocatalytic reduction with enhanced electrochemical oxidation-reduction properties for chlorophenols, Appl. Catal. B Environ. 203 (2017) 442–451, https://doi.org/10.1016/j.apcatb.2016.10.036.

[21] J.J. Li, H.L. Liu, X.W. Cheng, Q.H. Chen, Y.J. Xin, Z.P. Ma, W.X. Xu, J. Ma, N. Q. Ren, Preparation and characterization of palladium/polypyrrole/foam nickel electrode for electrocatalytic hydrodechlorination, Chem. Eng. J. 225 (2013) 489–498, https://doi.org/10.1016/j.cej.2013.01.049.

[22] Y.P. Hou, Z.B. Peng, L. Wang, Z.B. Yu, L.R. Huang, L.F. Sun, J. Huang, Efficient degradation of tetrabromobisphenol A via electrochemical sequential reduction-oxidation: degradation efficiency, intermediates, and pathway, J. Hazard. Mater. 343 (2018) 376–385, https://doi.org/10.1016/j.jhazmat.2017.10.004.

[23] G.M. Jiang, K.F. Wang, J.Y. Li, W.Y. Fu, Z.Y. Zhang, G. Johnson, X.S. Lv, Y. X. Zhang, S. Zhang, F. Dong, Electrocatalytic hydrodechlorination of 2,4-dichlorophenol over palladium nanoparticles and its pH-mediated tug-of-war with hydrogen evolution, Chem. Eng. J. 348 (2018) 26–34, https://doi.org/10.1016/j.cej.2018.04.173.

[24] R. Mao, C. Huang, X. Zhao, M. Ma, J.H. Qu, Dechlorination of triclosan by enhanced atomic hydrogen-mediated electrochemical reduction: Kinetics, mechanism, and toxicity assessment, Appl. Catal. B Environ. 241 (2019) 120–129, https://doi.org/10.1016/j.apcatb.2018.09.013.

[25] J.S. Zhou, Z.M. Lou, K.L. Yang, J. Xu, Y.Z. Li, Y.L. Liu, S.A. Baig, X.H. Xu, Electrocatalytic dechlorination of 2,4-dichlorobenzoic acid using different carbon-supported palladium moveable catalysts: adsorption and dechlorination activity, Appl. Catal. B Environ. 244 (2019) 215–224, https://doi.org/10.1016/j.apcatb.2018.11.052.

[26] Z.R. Sun, H.T. Shen, X.F. Wei, X. Hu, Electrocatalytic hydrogenolysis of chlorophenols in aqueous solution on $Pd_{58}Ni_{42}$ cathode modified with PPy and SDBS, Chem. Eng. J. 241 (2014) 433–442, https://doi.org/10.1016/j.cej.2013.10.066.

[27] Y. Liu, L. Liu, J. Shan, J.D. Zhang, Electrodeposition of palladium and reduced graphene oxide nanocomposites on foam-nickel electrode for electrocatalytic hydrodechlorination of 4-chlorophenol, J. Hazard. Mater. 290 (2015) 1–8, https://doi.org/10.1016/j.jhazmat.2015.02.016.

[28] J.J. Duan, S. Chen, C. Zhao, Ultrathin metal-organic framework array for efficient electrocatalytic water splitting, Nat. Commun. 8 (2017) 1–7, https://doi.org/10.1038/ncomms15341.

[29] J.B. Pan, B.H. Wang, J.B. Wang, H.Z. Ding, W. Zhou, X. Liu, J.R. Zhang, S. Shen, J. K. Guo, L. Chen, C.T. Au, L.L. Jiang, S.F. Yin, Activity and stability boosting of an oxygen-vacancy-rich $BiVO_4$ photoanode by NiFe-MOFs thin layer for water oxidation, Angew. Chem. Int. Ed. 60 (2021) 1433–1440, https://doi.org/10.1002/anie.202012550.

[30] Y. Xiao, X.Y. Guo, N.C. Yang, F.X. Zhang, Heterostructured MOFs photocatalysts for water splitting to produce hydrogen, J. Energy Chem. 58 (2021) 508–522, https://doi.org/10.1016/j.jechem.2020.10.008.

[31] Y.M. Sun, Z.Q. Xue, Q.L. Liu, Y.L. Jia, Y.L. Li, K. Liu, Y.Y. Lin, M. Liu, G.Q. Li, C. Y. Su, Modulating electronic structure of metal-organic frameworks by introducing atomically dispersed Ru for efficient hydrogen evolution, Nat. Commun. 12 (2021) 1–8, https://doi.org/10.1038/s41467-021-21595-5.

[32] W.R. Cheng, H.B. Zhang, D.Y. Luan, X.W. Lou, Exposing unsaturated Cu_1-O_2 sites in nanoscale Cu-MOF for efficient electrocatalytic hydrogen evolution, Sci. Adv. 7 (2021) eabg2580, https://doi.org/10.1126/sciadv.abg2580.

[33] Q.Y. Jiang, J. Xu, Z.Q. Li, C.H. Zhou, X. Chen, H.B. Meng, Y. Han, X.F. Shi, C. H. Zhan, Y.Q. Zhang, Q.F. Zhang, X.L. Jia, R.F. Zhang, Two-dimensional metal-organic framework nanosheet supported noble metal nanocrystals for high-efficiency water oxidation, Adv. Mater. Interfaces 8 (2021) 2002034, https://doi.org/10.1002/admi.202002034.

[34] S. Wan, J.D. Wu, D.P. Wang, H.L. Liu, Z.C. Zhang, J.M. Ma, C. Wang, Co/N-doped carbon nanotube arrays grown on 2D MOFs-derived matrix for boosting the oxygen reduction reaction in alkaline and acidic media, Chin. Chem. Lett. 32 (2021) 816–821, https://doi.org/10.1016/j.cclet.2020.04.040.

[35] W.C. Cui, H.Y. Bai, J.P. Shang, F.G. Wang, D.B. Xu, J.R. Ding, W.Q. Fan, W.D. Shi, Organic-inorganic hybrid-photoanode built from NiFe-MOF and TiO_2 for efficient PEC water splitting, Electrochim. Acta 349 (2020), 136383, https://doi.org/10.1016/j.electacta.2020.136383.

[36] P. Thangavel, M.R. Ha, S. Kumaraguru, A. Meena, A.N. Singh, A.M. Harzandi, K. S. Kim, Graphene-nanoplatelets-supported NiFe-MOF: high-efficiency and ultra-stable oxygen electrodes for sustained alkaline anion exchange membrane water electrolysis, Energ. Environ. Sci. 13 (2020) 3447–3458, https://doi.org/10.1039/D0EE00877J.

[37] J.W. Jia, L.F. Wei, Z.T. Guo, F. Li, C.L. Yu, T.X. Liang, In-situ controlled synthesis of NiFe MOF materials with excellent electrocatalytic performances for water splitting, Funct. Mater. Lett. 14 (2021) 2151011, https://doi.org/10.1142/S1793604721510115.

[38] J.J. Li, H. Wang, Z.Y. Qi, C. Ma, Z.H. Zhang, B. Zhao, L. Wang, H.W. Zhang, Y. T. Chong, X. Chen, X.W. Cheng, D.D. Dionysiou, Kinetics and mechanisms of electrocatalytic hydrodechlorination of diclofenac on Pd-Ni/PPy-rGO/Ni electrodes, Appl. Catal. B Environ. 268 (2020), 118696, https://doi.org/10.1016/j.apcatb.2020.118696.

[39] J.P. Perdew, K. Burke, M. Ernzerhof, Generalized gradient approximation made simple, Phys. Rev. Lett. 77 (1996) 3865–3868, https://doi.org/10.1103/PhysRevLett.77.3865.

[40] H.J. Monkhorst, J.D. Pack, Special points for Brillouin-zone integrations, Phys. Rev. B 13 (1976) 5188–5192, https://doi.org/10.1103/PhysRevB.13.5188.

[41] C.Y. He, J.Z. Tao, P.K. Shen, Solid synthesis of ultrathin palladium and its alloys' nanosheets on RGO with high catalytic activity for oxygen reduction reaction, ACS Catal. 8 (2018) 910–919, https://doi.org/10.1021/acscatal.7b03190.

[42] X.Y. Shu, Q. Yang, F.B. Yao, Y. Zhong, W.C. Ren, F. Chen, J. Sue, Y.H. Ma, Z.Y. Fe, D.B. Wang, X.M. Li, Electrocatalytic hydrodechlorination of 4-chlorophenol on Pd supported multi-walled carbon nanotubes particle electrodes, Chem. Eng. J. 358 (2019) 903–911, https://doi.org/10.1016/j.cej.2018.10.095.

[43] Y. Yang, X. Zhu, L. Wang, J. Lang, G. Yao, T. Qin, Z. Ren, L. Chen, X. Liu, W. Li, Y. Wan, Breaking scaling relationships in alkynol semi-hydrogenation by manipulating interstitial atoms in Pd with d-electron gain, Nat. Commun. 13 (2022) 2754, https://doi.org/10.1038/s41467-022-30540-z.

[44] Q. Li, X. Wang, Z. Xie, X. Peng, L. Guo, X. Yu, X. Yang, Z. Lu, X. Zhang, L. Li, Polar bonds induced strong Pd-support electronic interaction drives remarkably enhanced oxygen reduction activity and stability, Appl. Catal. B Environ. 305 (2022), 121020, https://doi.org/10.1016/j.apcatb.2021.121020.

[45] Y. Pan, Y.J. Chen, K.L. Wu, Z. Chen, S.J. Liu, X. Cao, W.O. Cheong, T. Meng, J. Luo, L.R. Zheng, C.G. Liu, D.S. Wang, Q. Peng, J. Li, C. Chen, Regulating the coordination structure of single-atom Fe-N_xC_y catalytic sites for benzene oxidation, Nat. Commun. 10 (2019) 4290, https://doi.org/10.1038/s41467-019-12362-8.

[46] Y.J. Chen, Z. Liu, S.J. Liu, Y.S. Cheng, C. Zhang, J.Q. Jiao, Y.K. Lu, W.H. Wang, K. A. Sun, X.L. Bi, A.Y. Han, B. Liu, Y. Pan, Y.Q. Liu, C.G. Liu, In-Situ doping-induced crystal form transition of amorphous Pd-P catalyst for robust electrocatalytic hydrodechlorination, Appl. Catal. B-Environ. 284 (2021), 119713, https://doi.org/10.1016/j.apcatb.2020.119713.

[47] R.S. Sahu, D.L. Li, R.A. Doong, Unveiling the hydrodechlorination of trichloroethylene by reduced graphene oxide supported bimetallic Fe/Ni nanoparticles, Chem. Eng. J. 334 (2018) 30–40, https://doi.org/10.1016/j.cej.2017.10.019.

[48] J.J. Li, C. Luan, Y.Q. Cui, H.X. Zhang, L. Wang, H. Wang, Z.H. Zhang, B. Zhao, H. W. Zhang, X.Y. Zhang, X.W. Cheng, Preparation and characterization of palladium/polyaniline/foamed nickel composite electrode for electrocatalytic dechlorination, Sep. Purif. Technol. 211 (2019) 198–206, https://doi.org/10.1016/j.seppur.2018.09.040.

[49] G.M. Jiang, M.N. Lan, Z.Y. Zhang, X.S. Lv, Z.M. Lou, X.H. Xu, F. Dong, S. Zhang, Identification of active hydrogen species on palladium nanoparticles for an enhanced electrocatalytic hydrodechlorination of 2,4-dichlorophenol in water, Environ. Sci. Technol. 51 (2017) 7599–7605, https://doi.org/10.1021/acs.est.7b01128.

[50] M.A. Arellano-Gonzalez, A.C. Texier, L. Lartundo-Rojas, I. Gonzalez, Electrochemical dechlorination of 2-chlorophenol on Pd/Ti, Ni/Ti and Pd-Ni alloy/Ti electrodes, J. Electrochem. Soc. 162 (2015) E223–E230, https://doi.org/10.1149/2.0021510jes.

[51] Z.M. Lou, J.S. Zhou, M. Sun, J. Xu, K.L. Yang, D. Lv, Y.P. Zhao, X.H. Xu, MnO_2 enhances electrocatalytic hydrodechlorination by Pd/Ni foam electrodes and reduces Pd needs, Chem. Eng. J. 352 (2018) 549–557, https://doi.org/10.1016/j.cej.2018.07.057.

[52] G.I. Danmaliki, T.A. Saleh, A.A. Shamsuddeen, Response surface methodology optimization of adsorptive desulfurization on nickel/activated carbon, Chem. Eng. J. 313 (2017) 993–1003, https://doi.org/10.1016/j.cej.2016.10.141.

[53] W.J. Xie, S.H. Yuan, X.H. Mao, W. Hu, P. Liao, M. Tong, A.N. Alshaulabkeh, Electrocatalytic activity of Pd-loaded Ti/TiO_2 nanotubes cathode for TCE reduction in groundwater, Water Res. 47 (2013) 3573–3582, https://doi.org/10.1016/j.watres.2013.04.004.

[54] C. Sun, Z.M. Lou, Y. Liu, R.Q. Fu, X.X. Zhou, Z. Zhang, S.A. Baig, X.H. Xu, Influence of environmental factors on the electrocatalytic dechlorination of 2,4-dichlorophenoxyacetic acid on nTiN doped Pd/Ni foam electrode, Chem. Eng. J. 281 (2015) 183–191, https://doi.org/10.1016/j.cej.2015.06.113.

[55] M. Chen, S. Shu, J. Li, X. Lv, F. Dong, G. Jiang, Activating palladium nanoparticles via a Mott-Schottky heterojunction in electrocatalytic hydrodechlorination reaction, J. Hazard. Mater. 389 (2020), 121876, https://doi.org/10.1016/j.jhazmat.2019.121876.

[56] K. Wang, S. Shu, M. Chen, J. Li, K. Zhou, J. Pan, X. Wang, X. Li, J. Sheng, F. Dong, G. Jiang, Pd-TiO_2 Schottky heterojunction catalyst boost the electrocatalytic hydrodechlorination reaction, Chem. Eng. J. 381 (2020), 122673, https://doi.org/10.1016/j.cej.2019.122673.

[57] S. Qin, C. Lei, X. Wang, W. Chen, B. Huang, Electrocatalytic activation of organic chlorides via direct and indirect electron transfer using atomic vacancy control of palladium-based catalyst, Cell. Rep. Phys. Sci. 3 (2022), 100713, https://doi.org/10.1016/j.xcrp.2021.100713.

[58] S. Pourrahimi, M. Rezaei, S.H. Tabaian, Electrochemical investigation of Pt–Pd nanoparticles formation–reduction kinetics and nucleation mechanisms, J. Appl. Electrochem 49 (2019) 1143–1155, https://doi.org/10.1007/s10800-019-01354-7.

[59] F. Spolaore, F. Tajoli, M.C. Dalconi, C. Hengst, F. Dornhaus, S. Gross, Pursuing unprecedented anisotropic morphologies of halide-free Pd nanoparticles by tuning their nucleation and growth, Dalton Trans. 51 (2022) 11476–11484, https://doi.org/10.1039/d2dt01498j.

[60] M. Rezaei, S.H. Tabaian, D.F. Haghshenas, Nucleation and growth of Pd nanoparticles during electrocrystallization on pencil graphite, Electrochim. Acta 59 (2012) 360–366, https://doi.org/10.1016/j.electacta.2011.10.081.

[61] I. Danaee, Kinetics and mechanism of palladium electrodeposition on graphite electrode by impedance and noise measurements, J. Electroanal. Chem. 662 (2011) 415–420, https://doi.org/10.1016/j.jelechem.2011.09.012.

[62] Y.-R. Kim, S.C.S. Lai, K. McKelvey, G. Zhang, D. Perry, T.S. Miller, P.R. Unwin, Nucleation and aggregative growth of palladium nanoparticles on carbon electrodes: experiment and kinetic model, J. Phys. Chem. C 119 (2015) 17389–17397, https://doi.org/10.1021/acs.jpcc.5b03513.

[63] M. Rezaei, S.H. Tabaian, D.F. Haghshenas, Electrochemical nucleation of palladium on graphene: a kinetic study with an emphasis on hydrogen co-reduction, Electrochim. Acta 87 (2013) 381–387, https://doi.org/10.1016/j.electacta.2012.09.092.

[64] S. Gu, X. Wang, Y. Wei, B. Fang, Mechanism for nucleation and growth of electrochemical deposition of palladium(II) on a platinum electrode in hydrochloric acid solution, Sci. China Chem. 57 (2013) 755–762, https://doi.org/10.1007/s11426-013-5026-2.

[65] Y. Shen, Y. Tong, J. Xu, S. Wang, J. Wang, T. Zeng, Z. He, W. Yang, S. Song, Ni-based layered metal-organic frameworks with palladium for electrochemical dechlorination, Appl. Catal. B Environ. 264 (2020), 118505, https://doi.org/10.1016/j.apcatb.2019.118505.

[66] N. Campagnol, T.R.C. Van Assche, M. Li, L. Stappers, M. Dincă, J.F.M. Denayer, K. Binnemans, D.E. De Vos, J. Fransaer, On the electrochemical deposition of metal–organic frameworks, J. Mater. Chem. A 4 (2016) 3914–3925, https://doi.org/10.1039/C5TA10782B.

[67] Y.Y. Peng, M.Y. Cui, Z.Y. Zhang, S. Shu, X.L. Shi, J.T. Brosnahan, C. Liu, Y.L. Zhang, P. Godbold, X.M. Zhang, F. Dong, G.M. Jiang, S. Zhang, Bimetallic composition-promoted electrocatalytic hydrodechlorination reaction on silver-palladium alloy nanoparticles, ACS Catal. 9 (2019) 10803–10811, https://doi.org/10.1021/acscatal.9b02282.

[68] R. Liu, H.C. Zhao, X.Y. Zhao, Z.L. He, Y.J. Lai, W.Y. Shan, D. Bekana, G. Li, J.F. Liu, Defect sites in ultrathin Pd nanowires facilitate the highly efficient electrochemical hydrodechlorination of pollutants by $H^*_{(ads)}$, Environ. Sci. Technol. 52 (2018) 9992–10002, https://doi.org/10.1021/acs.est.8b02740.

[69] J. Xu, X. Liu, Z. Cao, W.L. Bai, Q.Y. Shi, Y. Yang, Fast degradation, large capacity, and high electron efficiency of chloramphenicol removal by different carbon-

supported nanoscale zerovalent iron, J. Hazard. Mater. 384 (2020), 121253, https://doi.org/10.1016/j.jhazmat.2019.121253.
[70] X. Liu, Z. Cao, Z.L. Yuan, J. Zhang, X.P. Guo, Y. Yang, F. He, Y.P. Zhao, J. Xu, Insight into the kinetics and mechanism of removal of aqueous chlorinated nitroaromatic antibiotic chloramphenicol by nanoscale zero-valent iron, Chem. Eng. J. 334 (2018) 508–518, https://doi.org/10.1016/j.cej.2017.10.060.
[71] Y.Y. Jia, S.K. Khanal, L.W. Yin, L.P. Sun, H. Lu, Influence of ibuprofen and its biotransformation products on different biological sludge systems and ecosystem, Environ. Int. 146 (2021), 106265, https://doi.org/10.1016/j.envint.2020.106265.
[72] A. Abbaspour, F. Norouz-Sarvestani, High electrocatalytic effect of Au-Pd alloy nanoparticles electrodeposited on microwave assisted sol-gel-derived carbon ceramic electrode for hydrogen evolution reaction, Int. J. Hydrog. Energy 38 (2013) 1883–1891, https://doi.org/10.1016/j.ijhydene.2012.11.096.
[73] P. Wang, X.L. Shi, C.H. Fu, X.J. Li, J.X. Li, X.S. Lv, Y.H. Chu, F. Dong, G.M. Jiang, Strong pyrrolic-N-Pd interactions boost the electrocatalytic hydrodechlorination reaction on palladium nanoparticles, Nanoscale 12 (2020) 843–850, https://doi.org/10.1039/C9NR07528C.
[74] W.Y. Fu, S. Shu, J.X. Li, X.L. Shi, X.S. Lv, Y.X. Huang, F. Dong, G.M. Jiang, Identifying the rate-determining step of the electrocatalytic hydrodechlorination reaction on palladium nanoparticles, Nanoscale 11 (2019) 15892–15899, https://doi.org/10.1039/C9NR04634H.
[75] S.Y. Fan, X.Y. Li, J. Tan, L.B. Zeng, Z.F. Yin, M.O. Tade, S.M. Liu, Enhanced photoeletrocatalytic reduction dechlorinations of PCP by Ru-Pd BQDs anchored Titania NAEs composites with double Schottky junctions: First-principles evidence and experimental verifications, Appl. Catal. B-Environ. 227 (2018) 499–511, https://doi.org/10.1016/j.apcatb.2018.01.043.
[76] Y.H. Xu, Z.Q. Yao, Z.C. Mao, M.Q. Shi, X.Y. Zhang, F. Cheng, H.B. Yang, H.B. Tao, B. Liu, Single-Ni-atom catalyzes aqueous phase electrochemical reductive dechlorination reaction, Appl. Catal. B Environ. 277 (2020), 119057, https://doi.org/10.1016/j.apcatb.2020.119057.